U_P, $3U_P$, $11U_P$: ABOVE-THRESHOLD IONIZATION REVISITED

BAORUI YANG[a], K.J. SCHAFER[b], B. WALKER[a], K.C. KULANDER[b,c],
L.F. DIMAURO[a] AND P. AGOSTINI[d]

[a]Chemistry Department, Brookhaven National Laboratory
Upton, New York 11973, USA
[b]Lawrence Livermore National Laboratory, Livermore, California, USA
[c]Joint Institute for Laboratory Astrophysics, University of Colorado
Boulder, CO 80309, USA
[d]Service de Recherches sur les Surfaces et l'Irradiation de la Matière
Centre d'Etudes Nucléaires de Saclay, 91191 Gif-sur-Yvette, France

Angular distributions of very high energy photoelectrons from Xe and Kr, excited by a 50 ps, 1054 nm laser, are presented. In Xe strong, narrow structures 45° off the polarization axis appear on above-threshold ionization peaks within a limited energy range centered around $9U_P$, where U_P is the intensity-dependent ponderomotive energy. Under the same conditions the effect is much weaker in krypton. These structures are discussed using a very simple classical model as well as sophisticated single active electron calculations and the Keldysh–Faisal–Reiss theory. We conclude these structures are the result of single-electron dynamics involving rescattering of a tunneling component of the continuum wave function.

PACS numbers: 32.80.Rm, 31.90.+s, 32.80.Fb

1. Introduction

Many aspects of the interaction between a strong electromagnetic field and an atom have been enlightened by the momentum properties of the photoelectrons. The process known as above-threshold ionization (ATI) [1], in which the atom absorbs more photons than necessary to reach the continuum, could be revealed only by electron spectroscopy. At low intensity, where perturbation theory applies, ATI is described as a one-step multiphoton transition and the angular distributions (AD) of the photoelectrons are determined by the amplitudes of the different partial waves corresponding to the final state energy. For instance a two-photon ionization from an initial s-state results in a s- and a d-partial waves. In some cases one of the channels is dominant and the AD can be a pure, say s-wave. However, in most cases the AD is due to the interference between the various channels. As the number of channels increases exponentially with the number of absorbed photons, this analysis becomes rapidly untractable. However, on the basis of the

propensity rule that favors the high angular momenta when n increases, the AD are expected to become more peaked about the polarization vector for larger n's. This is also the intuitive prediction based on the quasi-static model, very successful in the long wavelength, high intensity limit, where the ionization is dominated by tunneling [2]. This model predicts that after the electron is freed from the atom, it is accelerated along the polarization by the laser's electric field. It is a more sophisticated version of the so-called "simpleman's theory" of ATI [3] in which the motion of the electron is treated by classical mechanics without reference to the physics of the ejection process. The averaged kinetic energy of a classical electron oscillating in the field*, U_P, as well as "magic" multipliers of U_P (3, 11, etc.), have clear physical interpretations in this theory.

It is the purpose of this paper to report very peculiar angular distributions recorded in high order ATI of xenon and krypton atoms by intense infrared picosecond pulses. These AD present features that are totally unexpected either in the perturbative or the classical picture. They have been obtained thanks to a high repetition rate (KHz) laser at Brookhaven National Laboratory. After a brief description of the experimental setup, the ADs are presented in the first section. The following sections are devoted to the discussion of the results with the help of different theoretical approaches: (i) simpleman's model, (ii) Keldysh–Faisal–Reiss theory and (iii) numerical solution of the time-dependent Schrödinger equation in the single-active electron (SAE) approximation [4].

2. Experiment

From an experimental perspective, the detection and resolution of high order ATI electrons have been limited by a combination of space-charge effects and low repetition rate laser sources (< 10 Hz). Recently [5], we have been able to increase our detection sensitivity to achieve several orders of magnitude in dynamic range by utilizing *kilohertz* repetition rate, gigawatt lasers. Consequently, it is now possible to explore the physics associated with very high order, strong field processes while keeping the measurement time within reasonable limits. In the experimental apparatus,.we use a 1054 nm, Nd:YLF laser system based on *cw*-pumped regenerative amplification which produces 4 mJ, 50 ps pulses at a repetition rate of > 1 kilohertz. The TEM$_{00}$ mode energy output is stable to $\pm 2\%$ and has been well characterized [6]. The light is focused by $f/4$ optics into a UHV system which consists of an electron and mass time-of-flight spectrometer viewing the interaction region 180° apart. The acceptance angle of the electron spectrometer is 4°. The electron ADs were collected by rotating the polarization direction of the laser relative to the space fixed spectrometer axis with a $\lambda/2$ plate. The $\lambda/2$ wave plate was optically characterized for phase distortions and the purity of the linear polarized light after the wave plate is measured to exceed 99%. The polar angle, θ, was varied over $> \pi$ radians to facilitate the detection of any asymmetries caused by imperfect alignment of optics. Target pressures were maintained such that the count rate never exceeded 0.25 electrons/shot (12–25 ions/shot) per data run, thus minimizing the effects of space charge. A data set (specific intensity or

---

*The ponderomotive energy, U_P, is defined in atomic units as $I/4\omega^2$, where I and ω are the laser intensity and frequency, respectively.

atom) was collected by randomizing the angular collection sequence at fixed target density and normalization was achieved by referencing the $0°$ electron spectrum after every data point (angle). The reproducibility of each data set was checked in at least three independent runs. Ionization of xenon into the $P_{3/2}$ continuum requires a minimum of $N = 11$ 1054 nm photons, which produces an electron with ≈ 0.8 eV kinetic energy. The energies of higher order peaks are given by $(Sh\nu + 0.8)$ eV, where $S = 1, 2, \ldots$ is the ATI order. In Fig. 1a we show a xenon
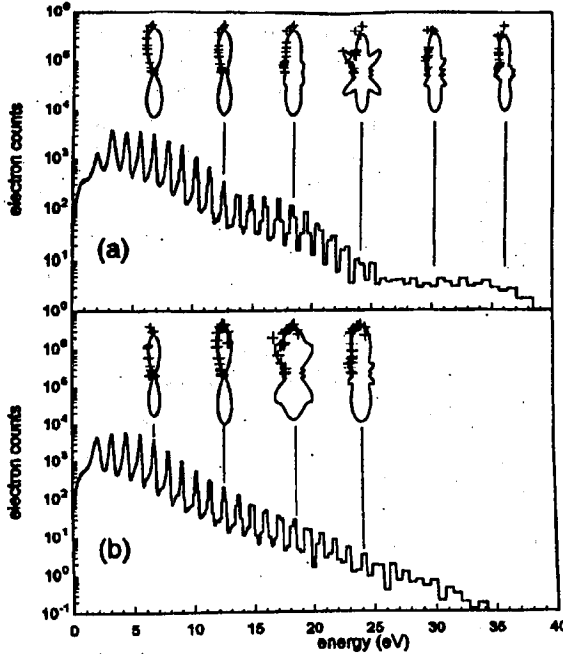

Fig. 1. The photoelectron energy spectrum of xenon with 50 ps, 1054 nm. Excitation at (a) 3×10^{13} W/cm^2 and (b) 1.9×10^{13} W/cm^2. The spectra are an average of 7.2 million laser shots. The insets are polar plots of the ADs of the $S = 5, 10, 15, \ldots$ ATI peaks. The solid line results from the Legendre fit and the raw data is shown as crosses.

electron energy spectrum recorded at the saturation intensity ($\approx 3 \times 10^{13}$ W/cm^2). The $S = 0$ and 1 peaks are suppressed due to ponderomotive channel closure, which provides an independent calibration of the laser intensity. The spectrum shows nicely resolved ATI out to the 21st order (≈ 25 eV). The electron peaks beyond 25 eV are instrumentally broadened but application of a retarding field reveals a resolvable series out to 40 eV. The dynamic counting range covers seven orders of magnitude. Also shown in Fig. 1a are representative ADs for different ATI orders $S = 5, 10, 15$. The data are fit by a sum of even Legendre polynomials

$$f(\theta) = \sum_{L=0}^{\infty} \beta_{2L} P_{2L}(\cos \theta).$$

The ADs for the first several peaks ($E < 15$ eV) are consistent with the expectations of our earlier discussion. The ionization is highly collimated along the z-axis with a slight narrowing with increasing S. However, as the order increases further the ADs for several peaks ($E > 15$ eV) exhibit unanticipated structure. For example, nearly one-half of the ionization signal in the $S = 20$ peak appears around 45° from the laser polarization axis [7]. Beyond these few structured peaks the ADs of the highest ATI orders observed (e.g., $S = 25$ and 30) abruptly return to the strongly aligned shape. In Fig. 1b, which is recorded at a lower intensity (1.9×10^{13} W/cm^2) the appearance of the ring structures has shifted to a lower ATI order (around $S = 15$). This energy shift is much larger than the corresponding 1.1 eV change in ponderomotive energy between these intensities. Although the detailed shapes of the ring structures and their directions of emission vary somewhat with intensity, their general appearance is relatively consistent. We find the structured ADs fall within a well-defined, intensity-dependent energy window. The intensity dependence of this window is illustrated in Fig. 2a. Here we show
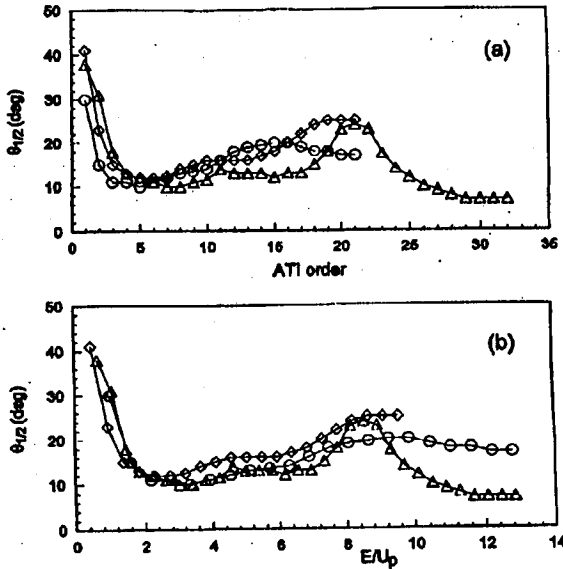

Fig. 2. Xe half-angles as functions of (a) ATI order and (b) electron energy, E, over ponderomotive energy, U_P, for various intensities. The value of U_P used for each curve is defined by the laser's peak intensity.

the ADs half-angle, $\theta_{1/2}$, defined by

$$\frac{\int_0^{\theta_{1/2}} f(\theta)\,d\theta}{\int_0^{\pi} f(\theta)\,d\theta} = 0.5$$

for each ATI peak. There is a region of rapid narrowing in the ADs for the lowest order ATI peaks (< 5) due to the ponderomotive scattering of low energy electrons in the long pulse limit ($t \gg 1$ ps). This well-known [8], intensity-dependent

macroscopic field effect is negligibly small for the higher energy ADs. The presence of ring structures causes a large increase in $\theta_{1/2}$. It is clear the position and width of the peak in the ADs half-angles are strongly intensity dependent. As the laser intensity is increased the rings move rapidly to higher ATI orders. A more revealing analysis of the intensity scaling is provided by plotting $\theta_{1/2}$ versus E/U_P the electron energy scaled by the ponderomotive energy. We show in Fig. 2b the clear and dramatic "rephasing" of the peaks in the AD half-angles *within a narrow energy range centered around* $9U_P$. The $9U_P$ scaling signifies that the rings cannot be due simply to a mechanism associated with the $1U_P$ shift of the ionization threshold.
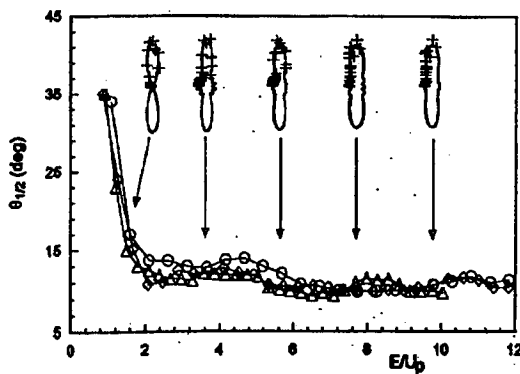

Fig. 3.   Half-angle as a function of U_P for krypton atom for various intensities.

Finally, in Fig. 3, we present the half-angle distributions for krypton. The broadening associated with the ring structures found in xenon are *conspicuously absent* at all intensities studied. The plot shows only the initial ponderomotive narrowing referred to above, followed by an almost constant half-angle out to beyond $10\,U_P$. The polar plots of representative ADs included as insets in Fig. 3 indicate some off-axis structure is present, but it is clearly much weaker in this atom.

3. Simpleman's theories

The simplest possible approach to ATI is to treat the free electron classically and neglect the Coulomb potential. The motion is then simply the superposition of an oscillatory and a drift motions. The drift velocity depends on the phase of the field at which the electron is born. Imposing a zero initial velocity yields for the instantaneous kinetic energy at time t

$$T(t,t_0) = 2U_P(\sin^2 \omega t + \sin^2 \omega t_0 - 2\sin \omega t \sin \omega t_0), \tag{1}$$

where t_0 is the time at which the electron is "born". The average kinetic energy is

$$T_{\mathrm{av}}(t_0) = 2U_P \left(\frac{1}{2} + \sin^2 \omega t_0 \right), \tag{2}$$

where U_P is the average kinetic energy of the oscillatory motion alone. If the electron is born exactly in phase with the field ($t_0 = 0$), the motion is purely oscillatory (Fig. 4).
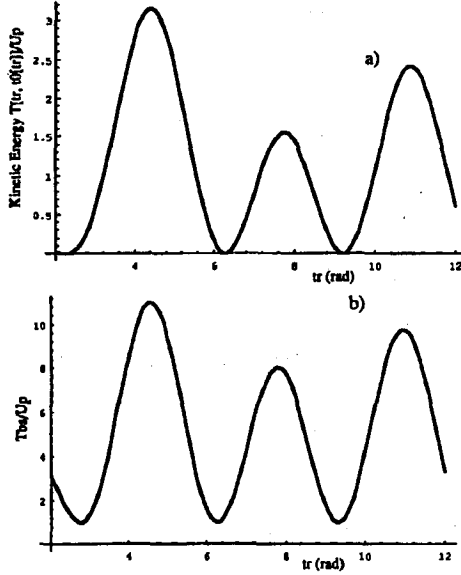

Fig. 4. (a) Kinetic energy of the electron as a function of the return time. The first maximum corresponds to $3.16\,U_P$ and the corresponding initial phase is 17.3 degree. (b) Average kinetic energy after a backscattering showing a maximum of $11U_P$.

It is interesting to determine the initial phase ωt_0 which corresponds to the maximum kinetic energy at the time the electron returns to the origin. Solving the equation of motion yields (for initial zero velocity)

$$\chi(t, t_0) = -\cos \omega t + \cos \omega t_0 - \omega(t - t_0) \sin \omega t_0. \tag{3}$$

The relationship between t_0 and the return time t_r should be given by $x(t_r, t_0) = 0$. Unfortunately this equation is not algebraic and cannot be solved. However, expanding $\cos t_0$ to second order and approximating $\sin t_0$ by t_0 provides a sufficient precision

$$t_0 = \frac{2t \pm \sqrt{4t_r^2 - 8(1 - \cos t_r)}}{2}.$$

Figure 4 shows a plot of the kinetic energy as a function of the return times. The maximum corresponds to $3.17\,U_P$ for a return time of 4.42 rad. The corresponding initial phase is 17.3 degree (from Eq. (3)). It has been pointed out by several authors that this is the origin of the cutoff IP $+ 3.17\,U_P$ (IP $=$ ionization potential) found in harmonics generation.

Here we are interested in another aspect of this return of the electron to the core. As proposed by Corkum [9], during the scattering on the core, the electron may absorb photons or, to keep the classical picture, some of its oscillation energy can be converted into translation energy. In particular, in the event of a backscattering at t_r, the average kinetic energy *after* t_r is

$$T_\mathrm{bs}(t_\mathrm{r}, t_0) = 2U_\mathrm{P}\left(\frac{1}{2} + 4\sin^2 \omega t_\mathrm{r} + \sin^2 \omega t_0 - 4\sin \omega t_\mathrm{r} \sin \omega t_0\right). \tag{4}$$

Using the relationship (3), one gets a maximum average kinetic energy of $11\,U_\mathrm{P}$. This value is closer to the maximum energy observed in experiments. Allowing scattering at a different angle results in a less efficient conversion of the oscillatory motion into translation motion and a lower kinetic energy. It is therefore attempting to speculate that the lobes observed around $9\,U_\mathrm{P}$ in the experiment are related to such a scattering. However, there is nothing in this crude model that justifies the presence of the lobes at $45°$.

4. Keldysh–Faisal–Reiss

A relatively simple one-electron model that incorporates effects beyond both perturbation theory and the quasi-static tunneling picture is based upon the theory of Keldysh [10]. Ionization is described in this model as a one step quantum transition from the initial ground state to a final (Volkov) state dressed by the laser field, neglecting any interaction with the ion core in the final state. Although it often underestimates the total ionization rate [11], it has shown some success in predicting low-order ATI spectra [12].

The total ionization probability writes

$$\sum_{n=n_0}^{\infty} \frac{\mathrm{d}W^{(n)}}{\mathrm{d}\hat{k}} = \frac{2\pi}{\hbar^3} \frac{1}{(2\pi)^3} \sum_{n=n_0}^{\infty} \left| (\varepsilon_n + \varepsilon_\mathrm{b}) J_n\left(\hat{k} \cdot \hat{\alpha}; \frac{U_\mathrm{P}}{2\hbar\omega}\right) \tilde{\Phi}(\tilde{k}) \right|^2, \tag{5}$$

where $\tilde{k}$ is the electron momentum, $\hat{\alpha}$ — the classical amplitude of the oscillation, ε_n — the electron kinetic energy ($n\hbar\omega - \varepsilon_\mathrm{b} - U_\mathrm{P}$) and ε_b — the binding energy. $J_n(a; b)$ is the generalized Bessel function defined as

$$J_n(a; b) = \sum_{m=-\infty}^{\infty} J_{n+2m}(a) J_m(b) \tag{6}$$

and $\tilde{\Phi}(\hat{k})$ is the Fourier transform of the ground state radial wave function.

ADs calculated in this manner are known to show structure due to the interference of final state amplitudes. We used three different ground state wave functions: hydrogenic $5p$ with xenon binding energy (12.13 eV); hydrogenic $4p$ with krypton binding energy (14 eV) and short range potential wave function with xenon binding energy. We calculated ATI spectra and ADs within this model for orders from 1 to 50. Since the function (5) is very sensitive to the values of the Bessel arguments, which contain intensity (through $\hat{\alpha}$) and U_P, we have averaged the result over a Gaussian distribution of intensity. Some results are shown in Figs. 5 and 6. Though some features of the experiment are present, e.g. prominent lobes in the ADs for certain orders (Fig. 5) there are many discrepancies: the overall shape of the ATI spectrum is wrong, dropping much too steeply at
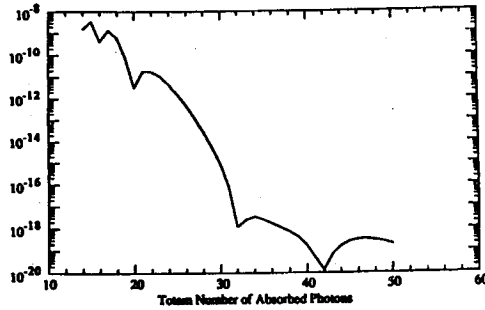
Fig. 5. Angular distribution for $n = 34$. For each angle the probability has been averaged over a Gaussian intensity distribution with a peak value of 3×10^{13} W/cm^{-2}. $\varepsilon_b = 12.13$ eV.
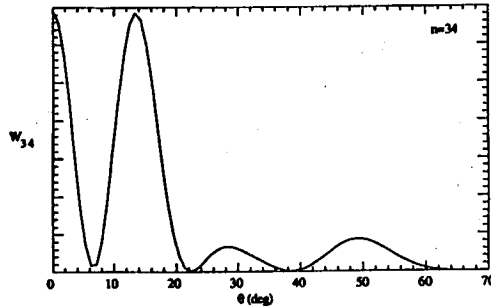

Fig. 6. ATI spectrum from SFA calculation. The same parameters as in Fig. 5.

high energy (Fig. 6) and there is no scaling with intensity akin to the $9\,U_P$ scaling seen experimentally. Furthermore, the dependence upon the initial state (the only atomic parameter in the theory) is very weak, in contrast to the dramatic difference between xenon and krypton illustrated in Figs. 1–3.

5. Time-dependent solution of the Schrödinger equation

A more sophisticated model which contains all of the physics of the tunnelling and Keldysh models and which can allow for the interaction of the electron with both the laser field and the ion core on an equal footing is needed. We have used the SAE model to carry out numerical calculations to obtain the xenon and krypton ADs. In this approach we calculate the response of each valence electron to a laser pulse in the effective field remaining atomic electrons, frozen in their ground state orbitals. The SAE has been shown to provide ionization rates and in particular ATI spectra for rare gases in the strong-field regime [13].

We analyze our results in the same manner as the experiments, calculating the half-angles for the ADs. These are shown for xenon in Fig. 7 for a number of different intensities as a function of E/U_P. In general, the qualitative behavior of the theoretical results is in excellent agreement with the measurements. In particular, the broadening of the ADs is confined to peaks near $9\,U_p$. (We have added
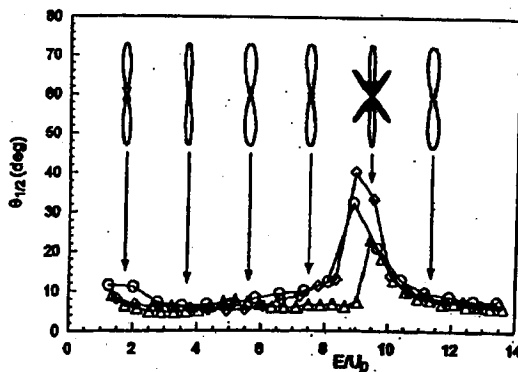
Fig. 7. Calculated Xe half-angles as functions of the electron energy, E, over pondero-motive energy, U_P, for various intensities. The insets are polar plots of the ADs of the $S = 5, 10, 15, \ldots$ ATI peaks.

$1U_p$ to the calculated electron energies because of the ponderomotive acceleration of the electrons present in these long pulse experiments). A similar calculation for krypton shows a significant reduction in magnitude of the effect, also in agreement with the experiments. We also include several polar plots of the calculated xenon ADs in Fig. 7. The general trend is an increasing elongation of the ADs along the z-axis. This is interrupted for only a few orders by the large, narrow side lobes near 45°. The appearance of the observed rings in the SAE calculations means that their explanation is most likely due to single electron ionization dynamics, specifically the interaction of the ionizing electron with the ion core. We are in the wavelength and intensity regime within which the ionization process is ceasing to be multiphoton absorption and beginning to be tunneling. By examination of the time-dependent wave function we observe two somewhat distinct "pieces" to the ionizing wave function: one which acquires energy while still close to the ion core (as in a multiphoton transition), and another, representing the contribution from tunneling, which enters the continuum far from the nucleus during a short time around the peak of the electric field. The wave function evolution reveals that electrons promoted to the continuum do interact strongly with the ion core as they leave the vicinity of the atom [14]. High energy ATI can come from electrons which tunnel into the continuum, get accelerated by the field and then rescattered from the core. At this time, there is a possibility that they will be backscattered. Classical simulations show that their resulting drift (cycle-averaged) energies can be as large as 8–$10\,U_p$. We believe that these back scattered electrons are responsible for the narrow side-structures in the high energy xenon ADs near $9\,U_p$. Because the scattering depends sensitively on the short range part of the potential, it is not surprising that the strength of the effect will depend on the particular atom studied. We also find that the tunneling portion of the wave function for krypton is greatly reduced and broadened by comparison with xenon in the experimental intensity range. Calculations using shorter wavelengths (and having consequently

clude the observed rings are the result of single-electron ionization and rescattering from the ion core.

Acknowledgments

References

[1] P. Agostini, F. Fabre, G. Mainfray, G. Petite, N.K. Rahman, *Phys. Rev. Lett.* **42**, 1127 (1979).

[2] P. Corkum, N. Burnett, F. Brunel, *Phys. Rev. Lett.* **62**, 1259 (1989); N.B. Delone, V.P. Krainov, *J. Opt. Soc. Am. B* **8**, 1207 (1991).

[3] II.B. van Linden van den Ileuvell, II.G. Muller, in: *Multiphoton Processes*, Eds. S.J. Smith, P.L. Knight, Cambridge University Press, Cambridge 1988, p. 25.

[4] K.C. Kulander, K.J. Schafer, J.L. Krause, *Int. J. Quantum Chem. Symp.* **25**, 415 (1991).

[5] L.F. DiMauro, D. Kim, M.W. Courtney, M. Anselment, *Phys. Rev. A* **38**, 2··· (1988).

[6] M. Saeed, D. Kim, L.F. DiMauro, *Appl. Opt.* **29**, 1752 (1990).

[7] D. Feldmann, private communication. Similar electron jets were seen in some earlier unpublished work on xenon using a Nd:YAG multimode, nanosecond laser.

[8] R.R. Freeman, P.II. Bucksbaum, T.J. McIlrath, *IEEE J. Quantum Electron.* **24**, 1461 (1988).

[9] P. Corkum (to be published).

[10] L.V. Keldysh, *Zh. Eksp. Teor. Fiz.* **47**, 1945 (1964); F.II.M. Faisal, *J. Phys. B* **6**, L89 (1973); II.R. Reiss, *Phys. Rev. A* **22**, 1786 (1980).

[11] II.G. Muller, P. Agostini, G. Petite, in: *Atoms in Intense Laser Fields*, Ed. M. Gavrila, Academic Press, Boston 1992, p. 1.

[12] II.R. Reiss *J. Opt. Soc. Am. B* **4**, 726 (1987).

[13] K.J. Schafer, Baorui Yang, L.F. DiMauro, K.C. Kulander, *Phys. Rev. Lett.* **70**, 1599 (1993).

[14] K.C. Kulander, K.J. Schafer, in: *Proc. Internat. Conf. on Multiphoton Processes VI*, Ed. D.K. Evans, World Scientific, Singapore 1993.